Developing Contacting Solutions for $Mg_2Si_{1-x}Sn_x$-based Thermoelectric Generators: Cu and $Ni_{45}Cu_{55}$ as Potential Contacting Electrodes

S. Ayachi[1*], *G. Castillo Hernandez*[1,2], *N.H. Pham*[1], *N. Farahi*[1], *E. Müller*[1,2], *and J. de Boor*[1]

[1]*German Aerospace Center, Institute of Materials Research, Dep. Of Thermoelectric Materials & Systems, Cologne, North Rhein-Westphalia, 51147, Germany,*

[2]*JLU Giessen, Institute of Inorganic and Analytical Chemistry, Giessen, Hessen, 35390, Germany*

Email addresses: Sahar.ayachi@dlr.de, Gustavo.Castillo-Hernandez@dlr.de, nganph38@gmail.com, nader.farahi@gmail.com, Eckhard.Mueller@dlr.de, Johannes.deBoor@dlr.de.*

Abstract

Magnesium silicides can be used for thermoelectric energy conversion, as high values of figure of merit *zT* were obtained for n-type (1.4 at 500 °C) and p-type (0.55 at 350 °C) materials. This, however, needs to be complemented by low resistive and stable contacting to ensure long-term thermogenerator operation and minimize losses. In this study, we selected Cu and $Ni_{45}Cu_{55}$ as contacting electrodes for their high electrical conductivity, similar coefficient of thermal expansion (CTE) and good adhesion to $Mg_2(Si,Sn)$. Both electrodes were joined to $Mg_2Si_{0.3}Sn_{0.7}$ pellets by hot pressing in a current-assisted press. Microstructural changes near the interface were analyzed using SEM/EDX analysis, and the specific electrical contact resistance r_c was estimated using a travelling potential probe combined with local Seebeck scanning. Good contacting was observed with both electrode materials. Results show low r_c with Cu, suitable for application, for both n-type and p-type silicides (< 10 μΩ·cm^2), with the occurrence of wide, highly conductive diffusion regions. $Ni_{45}Cu_{55}$ joining also showed relatively low r_c values (~ 30 μΩcm^2) for n- and p-type, but had a less inhomogeneous reaction layer. We also performed annealing experiments with Cu-joined samples at 450 °C for one week to investigate the evolution of the contact regions under working temperatures. r_c values increased (up to ~ 100 μΩcm^2) for annealed n-type samples, but remained low (< 10 μΩcm^2) for p-type. Therefore, Cu is a good contacting solution for p-type $Mg_2(Si,Sn)$, and a potential one for n-type if the diffusion causing contact property degradation can be prevented.

Keywords

Thermoelectrics; contacting; interface; electrical contact resistance; annealing.

I. Introduction

Thermoelectric (TE) materials can convert heat into electricity, providing an effective option for sustainable energy conversion in any system generating waste heat [1]. The performance of such TE materials is governed by the dimensionless figure of merit zT, defined as:

$$zT = \frac{\sigma S^2}{\kappa_{\mathrm{tot}}} T \qquad Eq.(1)$$

where σ is the electrical conductivity, S is the Seebeck coefficient, $\kappa_{\mathrm{tot}} = \kappa_{\mathrm{lat}} + \kappa_{\mathrm{el}}$ is the total thermal conductivity, which is the summation of the lattice thermal conductivity κ_{lat} and the electronic thermal conductivity κ_{el}, and T is the absolute temperature. Improved TE materials with optimized Seebeck coefficient and electrical and thermal conductivities are necessary for the development of high performance thermoelectric generators (TEG), as the efficiency of the TEGs depends on zT [2-3].

The efficiency of a TEG is governed by the efficiency of the n- and p-type legs, as well as the losses generated through different mechanisms, including thermal radiation, non-optimized current, material inhomogeneity of the legs, and electrical and thermal resistances between the TE material and the other interfaces such as metallic bridges. Resistances, being the major sources of loss, are being constantly investigated. Device efficiency is directly related to the device figure of merit which is defined as [4-5]:

$$ZT = \frac{{S_{\mathrm{dev}}}^2 T}{RK} = \frac{{S_{\mathrm{dev}}}^2 T}{(R_{\mathrm{leg}}+R_{\mathrm{c}})(K_{\mathrm{leg}}+K_{\mathrm{b}})} \qquad Eq.(2)$$

where S_{dev} is the Seebeck coefficient of the device, R the total electrical resistance and K the total thermal conductance. R_{leg} and, R_{c} are the electrical resistances of the TE legs and the contacts, K_{leg} is the thermal conductance of the TE legs and K_{b} the thermal conductance of the parasitic heat paths that bypass the legs. To stay within the focus of this paper, K_{b} will not be taken into consideration. More locations where contact resistances can appear come into play with more mature TEG prototypes, like the resistance between the contacting layers and the metallic bridges, but these can usually be neglected as they are metal-metal interfaces.

From $Eq.(2)$, it is clear that, for a high device efficiency, the electrical contact resistance (R_c) between the legs and the joining electrodes must be low. An acceptable ratio between contact resistance and the total resistance of the device is < 10% [6]. The joining should also be stable, and there should be no cracks or delamination between the electrode and the TE legs. This can be avoided by

choosing a joining electrode with a coefficient of thermal expansion (CTE) similar to that of the TE material.

The CTE matching assures a similar behaviour of both materials under the effect of temperature and minimises the occurrence of cracks [7] which can grow further under mechanical load or thermal cycling stress, leading to an eventual failure and breakage of the TE leg. Such cracks can also increase the internal resistance of the material, which wouldn't be beneficiary for the device performance.

Interdiffusion or local reactions often occur between the contacting electrode and the TE material, forming reaction layers. It is crucial to study these new layers in order to know their effect on the contact resistance, their inertness with respect to the composition and function of the TE material as well as their stability and development under thermal cycling or long-term annealing.

Among the efficient TE materials are magnesium silicide-based materials, which are cheap, non-toxic, abundant and environment friendly. They are also lightweight and possess good thermal and mechanical stability. These properties make them very attractive to industries such as aerospace and automotive [8]. The binary Mg_2Si has been thoroughly studied [9-10], and contact development has shown promising results. Ni worked well as a contacting electrode with Mg_2Si showing good adhesion, low specific contact resistance (< 10 $\mu\Omega cm^2$) and temperature stability [9, 11-14].

Cu has also been tested as a joining electrode for undoped Mg_2Si in ref. no [15]. The samples showed good adhesion of the interlayer and no cracks within the sample, but the obtained r_c was moderately high (~ 15 $m\Omega cm^2$) before and after thermal stability testing. It has also been stated, that, as the specific contact resistance depends on the carrier concentration, doping is expected to decrease r_c.

Solid solutions of Mg_2Si and Mg_2Sn show improved thermoelectric properties compared to the binary Mg_2Si [16]. In fact, n-type and p-type $Mg_2Si_{1-x}Sn_x$, with $0.6 < x < 0.7$, show zT_{max} ~ 1.4 and ~ 0.55, respectively, at mid-range temperatures (350 ~ 450 °C) [17-22]. These solid solutions become, then, more attractive for technological applications and device development. Traditionally, higher manganese silicides (HMS) have been used as the p-type counterpart to n-type $Mg_2(Si,Sn)$ materials due to their abundance, relatively good stability and high zT [23-24]. A few research papers also reported trials for module building using n-type Mg_2Si with p-type HMS materials [25-27]. However, due to the recently improved TE properties of p-type $Mg_2Si_{1-x}Sn_x$ materials [17], they are an excellent alternative to HMS HMS. In fact, using them as counterparts to n-type $Mg_2Si_{1-x}Sn_x$ reduces chemical complexity in further investigations and potentially simplifies contacting electrode selection and study.

So far, concerning contacting solutions, Ni and Ag have been tested as contacting electrodes for $Mg_2(Si,Sn)$ compounds. Ni joining results in small electrical contact resistance, but cracks were observed due to the high CTE mismatch between Ni and the TE materials (Ni: $13 \cdot 10^{-6}$ K^{-1},

$Mg_2Si_{0.4}Sn_{0.6}$: $18 \cdot 10^{-6}$ K^{-1}). As for Ag, low contact resistance was obtained only with p-type, while it was about one or two orders of magnitude higher for n-type [28].

In this work, n- and p-type $Mg_2Si_{1-x}Sn_x$ with $x = 0.7$ have been synthesized and joint with two different metallic electrodes, namely Cu and $Ni_{45}Cu_{55}$. The $Mg_2Si_{0.3}Sn_{0.7}$ composition has been chosen in particular because it shows the best TE properties for n-type. As p-type also has its best TE properties for compositions with $0.6 < x < 0.7$ [29], $x = 0.7$ has been selected for a better comparability of the results. It is also favourable to use similar n- and p-type materials as this simplifies contact development [30]. The selection of Cu and $Ni_{45}Cu_{55}$ was based on their CTE which matches with the selected TE material: Cu: $17 \cdot 10^{-6}$ K^{-1} [31], $Ni_{45}Cu_{55}$: $14.9 \cdot 10^{-6}$ K^{-1} [32], $Mg_2Si_{0.3}Sn_{0.7}$: $17.5 \cdot 10^{-6}$ K^{-1} [28].

The joining with both electrodes resulted in interfaces that were investigated with SEM/EDX, and the resistance of the contacts was determined from local mappings of the electrical potential and the Seebeck coefficient.

Results show good joining for both Cu and $Ni_{45}Cu_{55}$. As expected, Cu diffuses into the TE material, creating an inhomogeneous reaction layer and diffusion zones of different size. Nevertheless, the specific contact resistance is very low for both n- and p-types (< 10 $\mu\Omega cm^2$). Similarly, for $Ni_{45}Cu_{55}$, both Ni and Cu diffuse into the $Mg_2Si_{0.3}Sn_{0.7}$ matrix, with inhomogeneous interface and thick localized diffusion zones, but r_c is higher than that obtained from Cu contacting. This could be explained by the different resulting interfaces, as well as the differences in CTE matching between the electrodes and the TE material. From this perspective, Cu would be preferred as a potential contacting solution for technological optimization.

Annealing was also done for Cu joined samples. The obtained results show a proceeding diffusion of the electrode material into the TE material, and a low r_c for p-type materials. N-type materials, however, show a slightly different behaviour causing r_c results to be higher than for p-type.

II. Materials and methods

N- and p-type powder materials were synthesized with starting compositions of $Mg_{2.06}Si_{0.3}Sn_{0.665}Bi_{0.035}$ and $Mg_{1.97}Li_{0.03}Si_{0.3}Sn_{0.7,}$ respectively [33]. N-type samples were initially synthesized with 3% excess Mg to compensate for the Mg evaporation that occurs during the sintering time, which is double the sintering time needed for p-type samples. Both types were pressed in a 15 mm diameter graphite die at 700 °C for 1200 s for n- and 600 s for p-type, utilizing a direct sinter press DSP 510 SE from Dr. Fritsch GmbH, Fellbach, Germany, under vacuum, with a pressure of 66 MPa and a 1 K/s heating rate. These pressing conditions have been selected as to obtain optimal TE properties for both

compositions[34-35]. All studied samples had a high relative density (≥ 97%). Further details on measurements of Seebeck coefficient and electrical conductivity can be found in the literature [34-36].

Each sample was joined with three stacked disk shape foil layers on each side; each foil having a thickness of $\sim 50\ \mu m$. Such thickness of the electrodes was selected to simplify the contact resistance scanning measurements which have a limited lateral resolution. Cu (99,9%; Goodfellow) and $Ni_{45}Cu_{55}$ ($Ni_{45}Cu_{55}Fe_{0,0025}Mn_{0,0075}$; Goodfellow) foils were joined to the pressed pellets for 600 s at 600 °C and 550 °C respectively. These temperatures were chosen to be around half of the melting temperatures of the used materials (T_{melt} (Cu) $\approx\ 1085\ °C$, $T_{liquidus}$ ($Ni_{45}Cu_{55}$) $\approx\ 1300\ °C$). As $Ni_{45}Cu_{55}$ has a higher melting point, a higher joining temperature was expected. However, joining it 600°C led to melting and breakage of the sample; which is why a lower temperature was chosen. A more elaborate selection would have been based on thermodynamic data for Cu and Ni-Cu, but such data is not fully described in the ternary systems Cu-Mg-Sn and Cu-Mg-Si and to the best of our knowledge, no quaternary description is available. Therefore, the processing temperatures were determined from experimental results.

As joining temperatures are preferred to be as low as possible, 500 °C was also tried for both electrodes, but it was not sufficient for a good adhesion to the thermoelectric material. Delamination between individual foils of the joining electrodes was also observed at 500 °C. During all joining steps, no insulation layer to prevent current flow through the samples was applied.

The final samples were imaged along their cross section after being cut, grinded and polished. Microstructure and properties of the joining interfaces were investigated under SEM using Zeiss Ultra 55 equipped with an energy dispersive X-ray (EDX) detector with a 15 kV acceleration voltage. The spatial resolution corresponding to this voltage (E_0 = 15 keV) and to the density of the material used (ρ = 3.11 g cm^{-3}) is $R = \frac{0.064\ (E_0^{1.68} - E_c^{1.68})}{\rho} \approx 2$ µm, where E_c = 3.44 keV is the critical excitation energy [37]. Measured compositions were compared with expected phases from literature equilibrium diagrams for the ternary systems Cu-Mg-Si [38] and Cu-Mg-Sn [39], as well as the binary Ni-Si [40].

The contact resistance was calculated from the potential and Seebeck results obtained by an in-house built Potential & Seebeck Scanning Microprobe (PSM) [13, 41].

Annealing was also processed for Cu-joined samples to study the stability of the contact under set conditions of time and temperature. Each sample has been coated with a thick boron nitride layer to minimize Mg losses due to evaporation at high temperatures, sealed in quartz ampules filled with Argon, and then annealed for one week at 450 °C.

III. Results:

1. Microstructure:

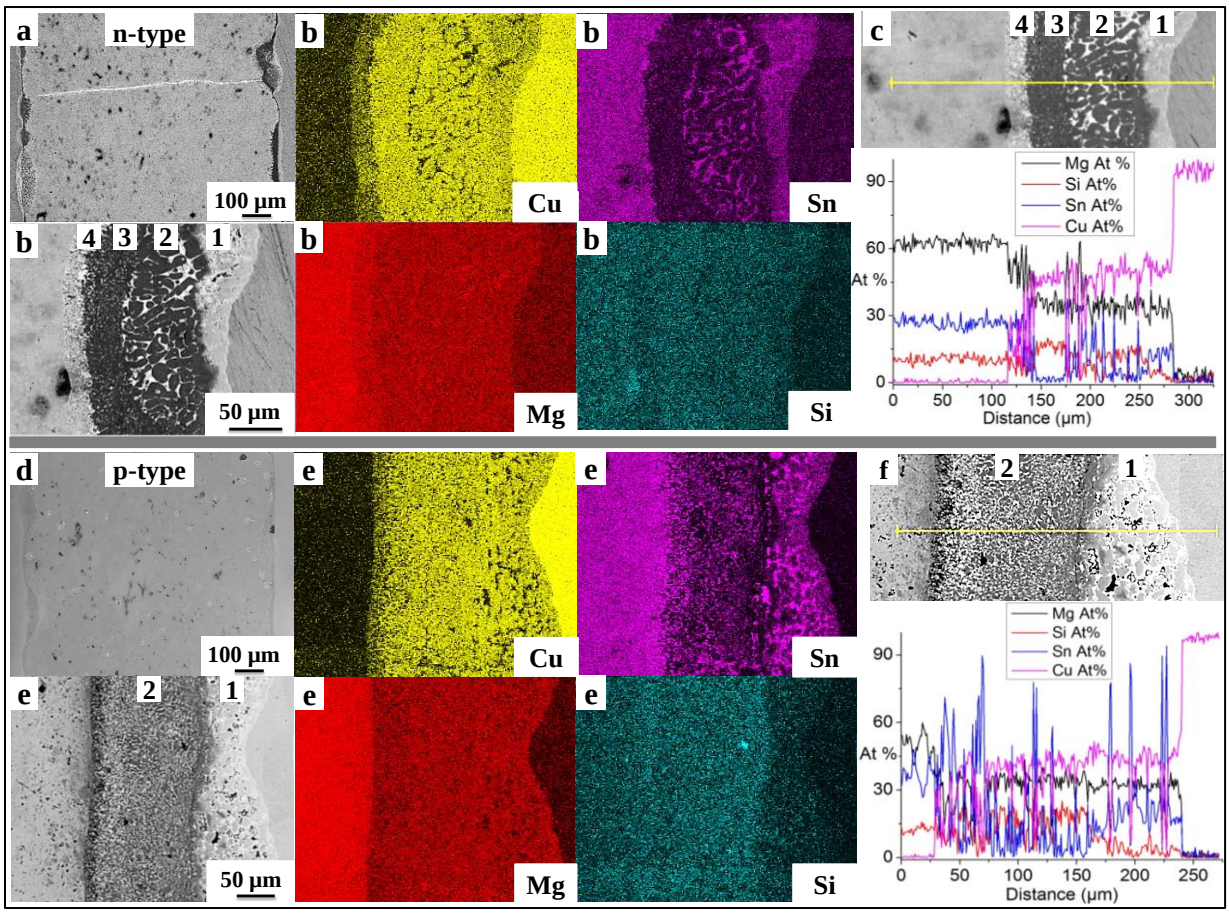

Figure 1 : *SEM - EDX results of Cu-joined n- (a–c) and p-type (d–f) $Mg_2Si_{0.3}Sn_{0.7}$: (a,d) overview of joined samples, (b,e) element mappings at an interface (c,f) line scans over interface layers.*

Figure 1 shows SEM - EDX results of both n- and p-type $Mg_2Si_{0.3}Sn_{0.7}$ samples joined with Cu. **Figures 1 (a)** and **(d)** show only selected sections of the samples; however, the visible size is $> 3\,mm^2$ and thus representative. The adhesion is good for both material types and neither delamination nor cracks between the electrodes and the TE material were observed (**Figure 1 (a)** and **(d)**). In fact, high magnification analysis proved that the darker "lines" along the interface between thermoelectric material and electrode are not cracks but thinner parts of the reaction layer. No cracks were also observed in the TE material itself, apart from one penetrating crack that can be seen on **Figure 1 (a)** as a horizontal channel running through the sample, which is believed to be rich in Mg_2Sn.

Both samples contain darker and brighter spots scattered over the TE $Mg_2Si_{0.3}Sn_{0.7}$ matrix. These are, respectively, Si-rich Mg_2(Si,Sn) phases and Sn segregates. The Si-rich phases are presumably residuals from the synthesis process, which has been confirmed through comparative SEM investigations before and after contacting [34]; while the Sn-rich phases appear in the second sintering step. In fact, these Sn-rich phases were most probably formed during the joining with Cu, under occurring current-induced temperature gradients that differently affect local inhomogeneities (local compositions, difference in grain size, micro-cracks…) in the sample, inducing Mg losses, and leaving the matrix locally rich in Sn.

Table 1: *EDX composition analysis results of interface layers 1–3 from* ***Figure 1 (c)*** *of the n-$Mg_2Si_{0.3}Sn_{0.7}$ joined with Cu.*

	Layer 1	Layer 2		Layer 3
		Dark segregates	Bright Region	
Cu (at.%)	~ 50	~ 50		~ 50
Mg (at.%)	~ 35	~ 35		~ 35
Sn (at.%)	~ 15	< 5		< 5
Si (at.%)	< 5	~ 15		~ 17
Likely phase	γ ($Cu_{1.55}MgSn_{0.45}$)	τ_1 ($Cu_{1.5}MgSi_{0.5}$)	Mg_2Sn	τ_1 ($Cu_{1.5}MgSi_{0.5}$)

The reaction layers forming from contacting both n-type and p-type $Mg_2Si_{0.3}Sn_{0.7}$ are thick and visible even at low magnification. They are uneven in thickness ($25 \sim 30\ \mu m$) and inhomogeneous in microstructure, with locally thicker zones of diffusion of $150 \sim 200\ \mu m$. Besides inhomogeneous current distributions during the pressing, the location of these thicker diffusion zones might be related to inhomogeneities of the thermoelectric material (local fluctuations in composition, varying grain sizes …) which serve as a seed for a faster reaction between electrode and thermoelectric material. EDX investigation of some of these diffusion zones is shown in shown in **Figure 1 (b), (c), (e)** and **(f)** and their descriptions are presented in **Table 1** and **Table 2**, respectively. Note that these selected diffusion zones in **(b)** and **(e)** are taken from parts of the samples that are not shown in **(a)** and **(d)**. EDX detected percentages that are lower than 5% were not taken into consideration due to detection limitation and potential errors and artefacts. References n° [38] and [39] were respectively used as references for interpretation and phase identification in the Cu-Mg-Si and Cu-Mg-Sn ternary phase diagrams.

For n-type (**Figure 1 (c)**), the diffusion zone shows dendritic growth from the Cu side inside the TE material. It contains different regions that can be categorized in four separate layers, each with a different composition. The outermost layer, numbered 1, has a thickness $\sim 25\ \mu m$. Combining composition results from EDX investigations and interpretations based on the used phase diagram [39], this layer seems to be mainly composed of one phase, the γ phase from the Cu-Mg-Sn phase diagram, which is $Cu_{2+x-y}Mg_{1-x}Sn_y$ with $x = 0$ and $y = 0.45$, giving the $Cu_{51.7}Mg_{33.3}Sn_{15}$ composition. This

phase is similar in structure to the Cu_2Mg binary but with Sn atoms sitting on some Cu sites. As Cu diffuses into the TE material matrix which is rich in Sn, nucleation and growth occur, leading to the formation of the γ phase in the first layer of the interface.

The following layer, numbered 2, is the thickest ($\sim 75\ \mu m$). The scatter in greyscale colours indicates that it is composed of more than one phase. In fact, from the EDX element mapping, the black spots are Cu segregates (dendrites) that have grown within a brighter matrix, which is Sn rich. From the line scan, one can see that where the Sn content peaks, that of Cu and Si drops. Mg content on the other hand doesn't vary a lot throughout the whole layer. This can be interpreted as the ternary τ_1 ($Cu_{1.5}MgSi_{0.5}$) phase for the darker segregates, and the Mg_2Sn matrix for the brighter area. Nucleation and growth of the τ_1 phase happen towards the TE material side of the γ phase, as Cu continues to diffuse inside the TE material.

The third layer has a thickness of $\sim 30\ \mu m$ and it seems to be similar in composition to the first layer as it is mainly composed of three elements but with Sn being replaced by Si. The stoichiometry (see **Table 1**) fits with the ternary τ_1 phase ($Cu_{1.5}MgSi_{0.5}$) of the Cu-Mg-Si system.

The fourth layer, adjacent to the TE material, is the thinnest one ($\sim 20\ \mu m$) and most complicated in composition. All four elements exist with non-negligible atomic percentage (≥ 10 at. %), which make phase recognition difficult. Nevertheless, a closer investigation of the line scan across this layer as well as the correlation with the SEM data shows the existence of at least two phases, potentially $Mg_2Si_{0.3}Sn_{0.7}$ and the τ_1 phase ($Cu_{1.5}MgSi_{0.5}$). This is similar with the phases composing layer 2 (τ_1 and Mg_2Sn), but as we are closer to the TE material side, the concentration in Si is higher.

Cu-joined p-type investigations of a localized diffusion zone are presented in **Figure 1 (e)** and **(f)**. This diffusion zone has a thickness of $\sim 200\ \mu m$ and, similar to the n-type case, it is composed of four layers. Two of these layers are very thin ($< 10\ \mu m$) and will therefore be disregarded in the following analysis.

Table 2: *EDX composition analysis results of interfaces of p-type $Mg_2Si_{0.3}Sn_{0.7}$ joined with Cu*

	Layer 1	Layer 2
Cu (at.%)	~ 45	~ 45
Mg (at.%)	~ 35	~ 35
Sn (at.%)	~ 15 ~ 20	< 5
Si (at.%)	< 5	~ 15 ~ 20
Possible phases	γ + Sn / Mg_2Sn	τ_1 + Sn / Mg_2Sn

From the element mapping and the line scan, Cu and Mg are roughly constant throughout the layer scheme, except for the Sn-rich spots. On the other hand, Si and mostly Sn fluctuate a lot. The outermost layer numbered 1 is mainly composed of Cu, Mg and Sn, and the difference in greyscale

colours indicates the coexistence of more than one phase. The atomic compositions match with the ternary γ phase observed in layer 1 of **Figure 1 (b)**. The higher Sn concentrations, though, can be related to elemental Sn or a mixture of Mg_2Sn and elemental Sn that accumulates as the brighter islands visible in the SEM figures. This is in line with the observation of high Sn content (peaks) in the corresponding line scan.

Layer number 2 has at least two phases: the darker part that is mostly Cu, Mg and Si, and the brighter spots are, here again, Sn-rich segregates. In this region, the atomic compositions correspond to the τ_1 phase that was also observed in the n-type case. Sn line scan in **Figure 1 (f)** oscillates a lot between values $\leq 5\,\text{at.}\%$ and $\geq 80\,\text{at.}\%$, which correlates very well with the scattered appearance of the bright Sn-rich microstructures.

Figure 2 is a composition mapping that shows a section of a diffusion zone from the reaction layer of p-type with Cu under very high magnification. The dendritic growth of Cu-containing phases as it precipitates out of the matrix is clearly visible as the grey elongated shapes seen in the figure below. These dendrites contain about $50\,at.\%$ Cu, $30\,at.\%$ Mg and $20\,at.\%$ Si, but no Sn. Such stoichiometry corresponds to the τ_1 phase from the Cu-Mg-Si ternary system, already mentioned above. Sn is mainly filling the white areas around the dendrites, with measured atomic percentages varying between 50% and 80%. This proves that the Cu-Mg-Si phases are more stable than the Cu-Mg-Sn phases, which explains the favourable crystallization of the τ_1 phase and the left out elemental Sn. As Mg seems to be also present in these white areas with concentrations between 30 and 50%, whereas Si and Cu are not, the matrix surrounding the dendrites could be a mix of elemental Sn and some Mg_2Sn. **Figure 2** also shows some local black spots, which seem to contain $\sim 90\%$ of Sn according to the composition mapping. As Sn is the heaviest element in the matrix and is so expected to be the brightest, these black spots are then presumably pores and the readings of the mapping at these black spots are artefacts. Further work and better spatial resolution are required to confirm whether it is Sn or Mg_2Sn (or both).

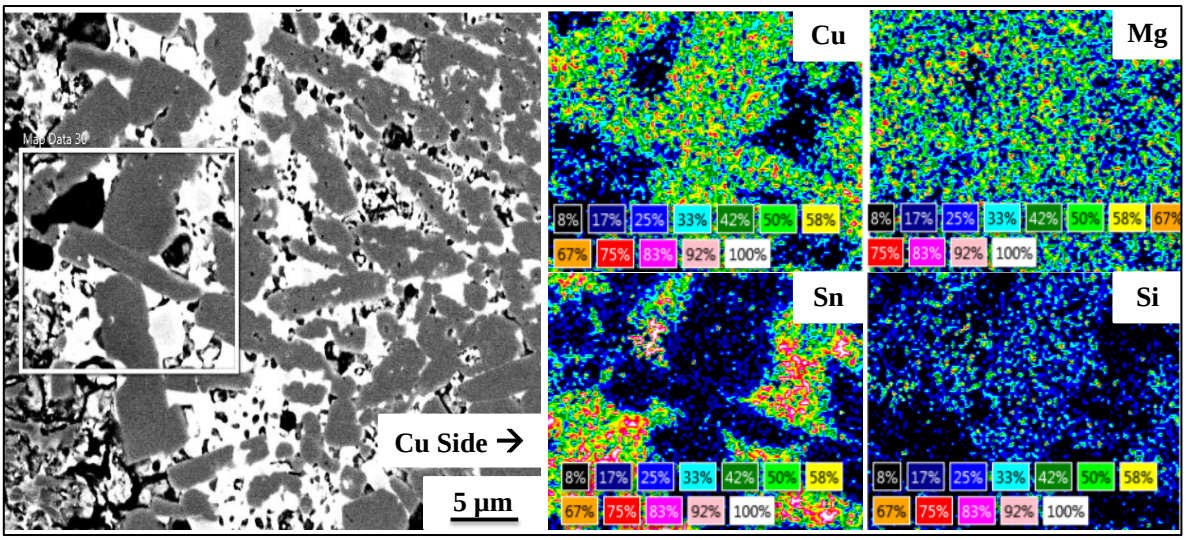

***Figure 2**: Composition mapping on the reaction layer of Cu-joined p-type $Mg_2Si_{0.3}Sn_{0.7}$ (Cu on right hand side)*

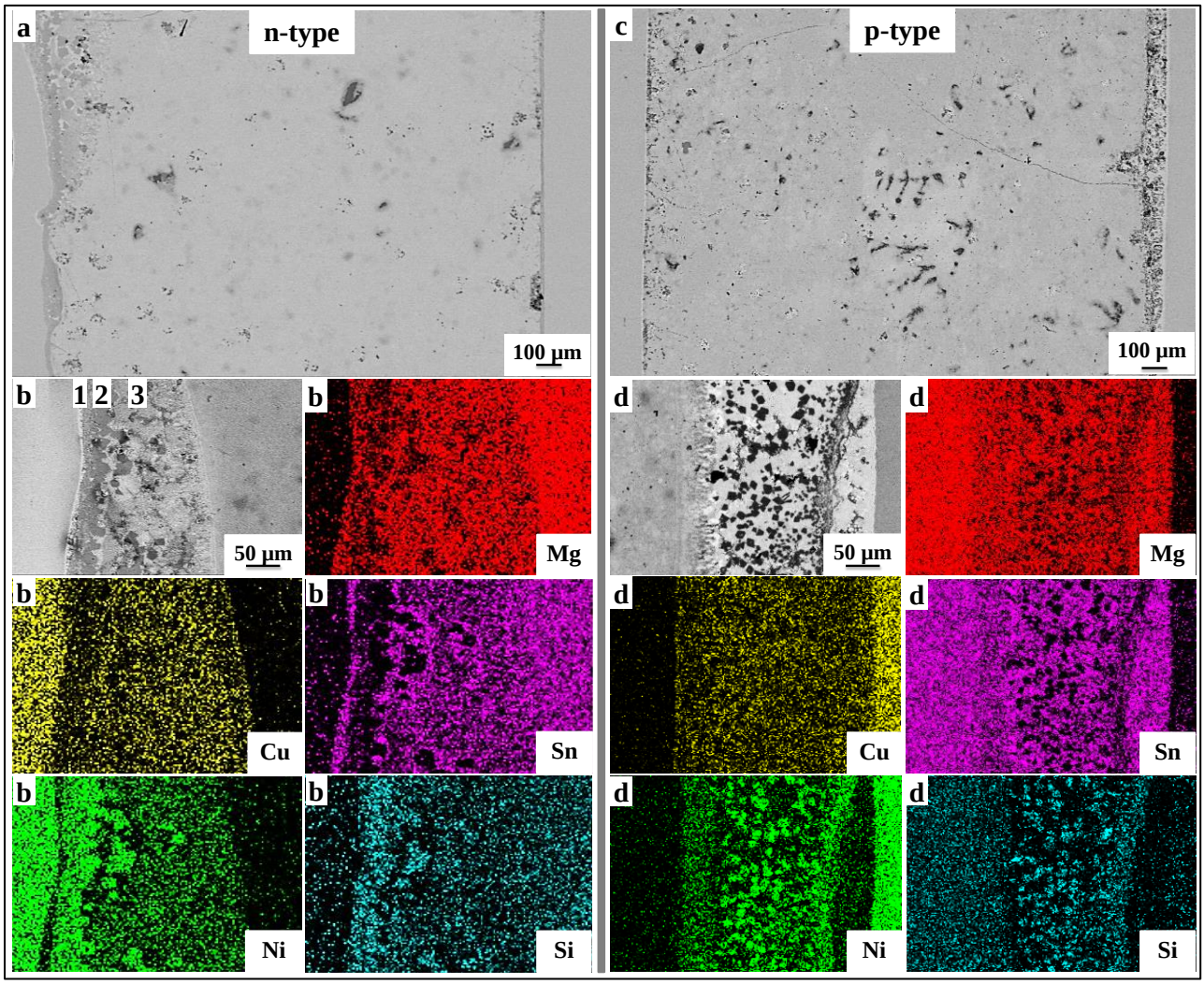

***Figure 3**: SEM - EDX results of a $Ni_{45}Cu_{55}$-joined n- and p-type $Mg_2Si_{0.3}Sn_{0.7}$: (a) overview of joined n-type, (b) overview of joined p-type, (c) element mapping on interface of n-type, (d) element mapping on interface of p-type*

Figure 3 shows SEM/EDX investigations of the joining of $Ni_{45}Cu_{55}$ with n- and p-type $Mg_2Si_{0.3}Sn_{0.7}$ doped with Bi and Li, respectively. Similar to the case of Cu joining, no delamination was observed. The dark Si-rich phases due to the synthesis process are visibly scattered across the samples, but no Sn-rich segregates were observed. As the appearance of such phases in the Cu joined cases has been correlated with temperature gradients and local overheating inside the sintering chamber, their absence in this $Ni_{45}Cu_{55}$ joining case could be due to the lower joining temperature (550°C for $Ni_{45}Cu_{55}$, 600°C for Cu) and therefore lower local overheating. **Figure 3 (c)** also shows some cracks inside the p-type TE material, starting from the reaction layers towards the inside of the material.

An interesting feature occurring with $Ni_{45}Cu_{55}$ and which has not been seen with Cu is the difference between the reaction layers on each side of the samples. As **Figure 3 (a)** and **(c)** show, the interface is much thicker on one side of each sample than on the other. The thin layers have a thickness of 15 ~ 20 µm, while the thick ones have a thickness of $150 \sim 190\ \mu m$, are inhomogeneous and contain different regions.

Figure 3 (b) presents an EDX element mapping of the interface of the joint n-type. Both thin and thick layer have a similar composition and microstructure, so only an analysis of the thick side is presented here. The first region labeled 1 on the figure, a very thin layer closest to $Ni_{45}Cu_{55}$ side is mainly Cu, Mg and Sn, but no Ni or Si. The layer doesn´t look single phased, so it could potentially contain the binary Mg_2Sn with some elemental Cu, or it could also be a mix of Mg_2Sn and a Cu-Mg-Sn ternary phase. As the γ ($Cu_{1.55}MgSn_{0.45}$) phase occurred often in the case of Cu contacting, it could be the existing ternary phase here, and this first layer would then contain Mg_2Sn and γ.

The following layer, layer 2, is a larger Ni- and Si- rich layer, and the third and last layer, which is the thickest and closest to TE material, contains all five elements, with square-shaped precipitates of Ni and Si. A similar description can be made for the interface of the joint p-type, as can be seen from **Figure 3 (d)**. Here also, we can see a first layer that doesn´t contain any Ni or Si, and could possibly be Mg_2Sn + (Sn,Cu). The Ni-Si accumulations also exist in an Mg-Cu-Sn matrix, and occur even more often than in the case of n-type.

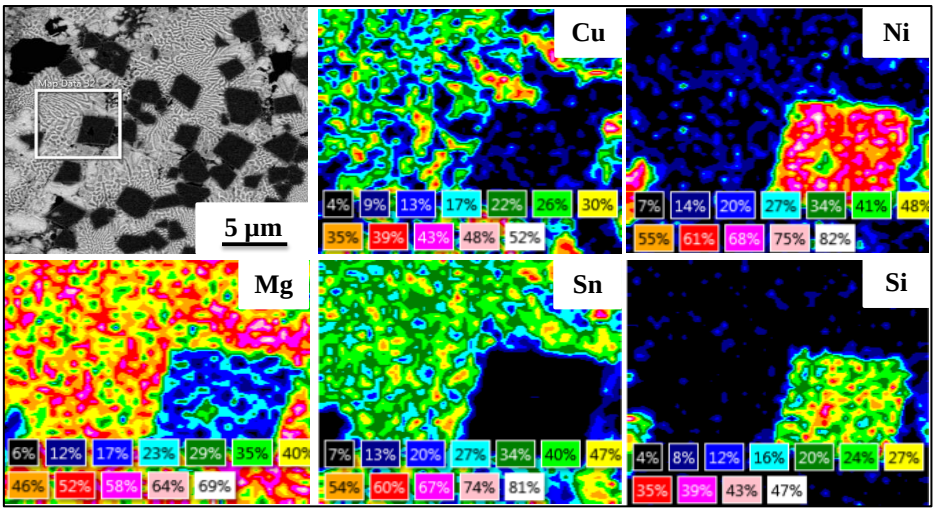

***Figure 4**: Composition mapping on interface of $Ni_{45}Cu_{55}$-joined p-type $Mg_2Si_{0.3}Sn_{0.7}$*

To confirm the microstructure of these Ni-Si accumulations, composition mapping in the middle of the interface of the joined p-type sample is presented in **Figure 4**. The obtained data show that these square shapes have an atomic composition of $50 \sim 75\ at.\%$ Ni and $20 \sim 35\ at.\%\ Si$. Such Ni-Si phase formation has been observed in the literature [14] before, in Mg_2Si/Ni contacts where a single reaction layer of $Ni_{31}Si_{12}$ (Ni $\sim 73\ at.\%$ and Si $\sim 27\ at.\%$) was identified. The Ni-Si precipitates shown in **Figure 4** are surrounded by a eutectic-like morphology with an average composition of $\sim 50\ at.\%$ Mg, $\sim 35\ at.\%$ Sn and $\sim 20\ at.\%$ Cu which falls in a non-fully determined region of the Cu-Mg-Sn equilibrium diagram. As the micrographs show at least two different phases, it could be τ_1-CuMgSn with the binary Mg_2Sn.

2. Electrical Contact Resistance:

The resulting contact resistance is calculated using the electrical potential data obtained from the PSM measurements, as well as the properties of the employed TE material. In case of a homogeneous current density $j = {}^{I}/_{A}$ passing through the sample and the contact, the bulk contact resistance R_c can be obtained using this equation:

$$R_c = \frac{V_{elec} - V_{TE}}{I} \qquad \text{(Eq.3)}$$

where V_{elec} and V_{TE} are the local voltages measured on the electrode and the TE material, respectively, on both sides of the interface. Previous literature [15, 42-45] also uses the same equation.

However, the homogeneity of the electrical field can be distorted by irregularities in the material and non-homogeneous interfaces [45]. Given the complex and sub-structured interfaces observed in the samples, a homogeneous current density distribution can therefore not be assumed a priori. If one assumes that the current density j is approximately constant in the direction of the line scan (which is a less strict assumption) j can be estimated using the properties of the TE material, where the specific contact resistance $r_c = R_c * A$ is

$$r_c = \frac{V_{elec} - V_{TE}}{j} \quad \text{(Eq.4)}$$

with

$$j = \frac{\Delta V_{TE}}{R_{TE} * A} \quad \text{(Eq.5)}$$

$$R_{TE} = \frac{l_{TE}}{A \sigma_{TE}} \quad \text{(Eq.6)}$$

where ΔV_{TE} and R_{TE} are the voltage and the resistance across the material, l_{TE} and σ_{TE} are its length and electrical conductivity, respectively. The average cross section A for all measured samples is around 3.5 mm^2.

Thus, r_c can be estimated from

$$r_c = \frac{(V_{elec} - V_{TE})\, l_{TE}}{\Delta V_{TE} * \sigma_{TE}} \quad \text{(Eq.7)}$$

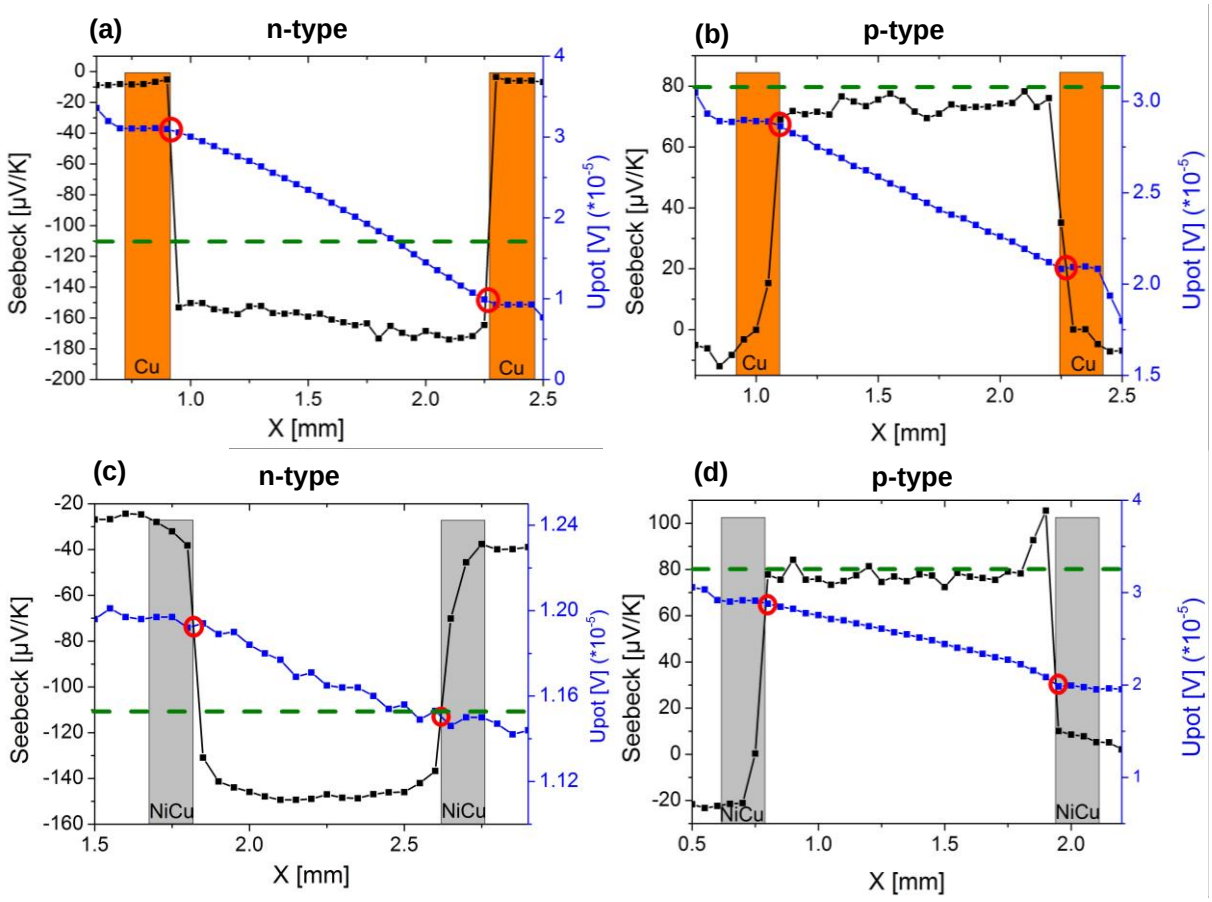

***Figure 5**: PSM graphs of (a): n-type $Mg_2Si_{0.3}Sn_{0.7}$ joined with Cu, (b): p-type with Cu, (c): n-type with $Ni_{45}Cu_{55}$ and (d): p-type with $Ni_{45}Cu_{55}$. The dashed green lines indicate the value of the sample´s Seebeck coefficient before joining.*

Figure 5 shows typical results of line scans of the Seebeck coefficient and the electrical potential obtained from PSM measurements. The drop in the Seebeck graph is used to determine the position of the interface. From that position, the values of the voltages V_{elec} and V_{TE} are read from the U graph at the positions just before and after the interface. Several line scans are used to obtain an average result for r_c.

All four graphs shown above display a smooth decrease in U towards the low potential side within the sample. The absence of sudden potential drops at the interface positions (marked with red circles) indicates that the contact resistance is low.

Quantitative results for r_c using the material properties $(Eq. 7)$ and r_c assuming constant current density $(Eq. 3)$ are presented in **Table 3**.

Table 3: *Specific contact resistance values of n- and p-type $Mg_2Si_{0.3}Sn_{0.7}$ joined with Cu and $Ni_{45}Cu_{55}$. The relative measurement uncertainty is the standard deviation of all line scans for each sample*

Sample	r_c $(Eq.7)$ / $(\mu\Omega cm^2)$	r_c $(Eq.3)$ / $(\mu\Omega cm^2)$
n + Cu	6 ± 4	9 ± 6
p + Cu	8 ± 5	3 ± 2
n + $Ni_{45}Cu_{55}$	24 ± 17	4 ± 3
p + $Ni_{45}Cu_{55}$ (thin interface side)	11 ± 6	15 ± 8
p + $Ni_{45}Cu_{55}$ (thick interface side)	53 ± 26	73 ± 36

As shown in the table, r_c $(Eq.7)$ values are indeed relatively low, especially for the case of Cu joining.

Note that the change in potential across the sample is very low and that the signal is noisy for n-type contacted with $Ni_{45}Cu_{55}$ (**Figure 5 (c)**), which indicates a low current density in the measurement region.

For $Ni_{45}Cu_{55}$ with p-type samples, r_c was around 6 times higher than Cu joined with p-type. The values for the thick and thin layer sides were respectively $\sim$ 11 $\mu\Omega cm^2$ and 53 $\mu\Omega cm^2$ $(Eq.7)$ yielding an average r_c value of $\sim$ 30 $\mu\Omega cm^2$. Such difference can be correlated with the corresponding *S* graph in **Figure 5** where a higher peak is visible on the right-hand side of the graph, indicating a local change of the material properties at the position of the thick interlayer.

Comparing results from r_c $(Eq.7)$ and r_c $(Eq.3)$, all obtained values are similar, except for n-type joint with $Ni_{45}Cu_{55}$. For this sample, further SEM/EDX investigations have shown the existence of "diffusion channels" of $\sim 100\ \mu m$ width running between interfaces on both sides. These channels are mainly composed of metallic phases that create a short circuit in the samples, which explains the observed small change in potential and increases measurement uncertainties due to line to line differences. In general, if the material properties are known, $Eq.7$ is more reliable than $Eq.3$ as its applicability requires fewer conditions.

Besides the low contact resistances, a change in the TE properties has been observed in n-type samples joint with both Cu and $Ni_{45}Cu_{55}$. In fact, **Figure 5 (a)** and **(c)** show that the *S* values of the samples after joining are $-150 \sim -160\ \mu V/K$, while the initial value before contacting was $\sim -110\ \mu V/K$ (marked with green dashed line). Such change in *S* is not observed with p-type samples where the *S* value remains constant after joining ($\sim 80\ \mu V/K$). For this reason, σ_{TE} has been measured again for n-type contacted samples and implemented in $Eq.7$ to obtain correct r_c values [46].

Table 4 below summarizes the changes in S values and provides estimations for the corresponding carrier concentrations. As $Mg_2(Si,Sn)$ is a well-studied material system and it had been shown that single parabolic band model can be used to describe the electrical transport for both n-type [22, 47-48] and p-type [17, 19, 29], we used a well-established SPB model that was developed in our group to estimate carrier concentration values[29]. For these calculations, we assume $\boldsymbol{m_D^*} = 2.5$ [49] for n-type samples and $\boldsymbol{m_D^*} = 1.5$ for p-type samples [29] and use $\mathbf{S} = \frac{k_b}{e}\left(\frac{2F_1}{F_0} - \eta\right)$ $\boldsymbol{and}$ $\boldsymbol{n} = \mathbf{4}\boldsymbol{\pi}\left(\frac{\mathbf{2}\boldsymbol{m_D^*}\boldsymbol{k_{b_B}}\boldsymbol{T}}{\boldsymbol{h^2}}\right)^{\mathbf{1.5}} \boldsymbol{F_{\frac{1}{2}}}(\boldsymbol{\eta})$ to estimate the carrier concentration n from the measured Seebeck coefficient.

The table also presents the ratios of electrical contact resistances to the resistance of the thermoelectric material with assumed dimensions of length $l = 5\ mm$ and area $A = 1\ cm^2$. As the actual samples used were not designed for module building, they had different thicknesses.

Table 4: *Seebeck coefficients S, estimated carrier concentrations* $\boldsymbol{n}$ *and ratios of contact resistance to material resistance for contacted samples.*

Type	Contact	S $(\mu V/K)$	n (cm^{-3})	σ (S/cm)	r_c $(\mu\Omega cm^2))$	R_{TE} $(\times 10^{-4}\Omega)$	$2r_c/(A \times R_{TE})$
n	None	-110	2.9×10^{20}	1851	--	2.7	--
	Cu	-160	1.38×10^{20}	710	6 ± 4	7.04	1.70 %
	$Ni_{45}Cu_{55}$	-160	1.38×10^{20}	710	24 ± 17	7.04	6.82 %
p	None	80	2.35×10^{20}	683	--	4.39	--
	Cu				8 ± 5		3.64 %
	$Ni_{45}Cu_{55}$ (thin side)				11 ± 6		5.01 %
	$Ni_{45}Cu_{55}$ (thick side)				53 ± 26		24.14 %

It can be seen that the estimated reduction in carrier concentration is significant and in line with the observed reduction in electrical conductivity. The ratio of contact to material resistances is in the lower percentage range for Cu and n-type contacted with $Ni_{45}Cu_{55}$, and somewhat higher for p-type contacted with $Ni_{45}Cu_{55}$.

3. Annealing:

As Cu contacted samples show better r_c results, they have been annealed at 450 °C for one week to study their thermal stability under thermal treatment. This temperature has been selected because it is around the actual working temperature of the final $Mg_2Si_{1-x}Sn_x$-based thermoelectric device.

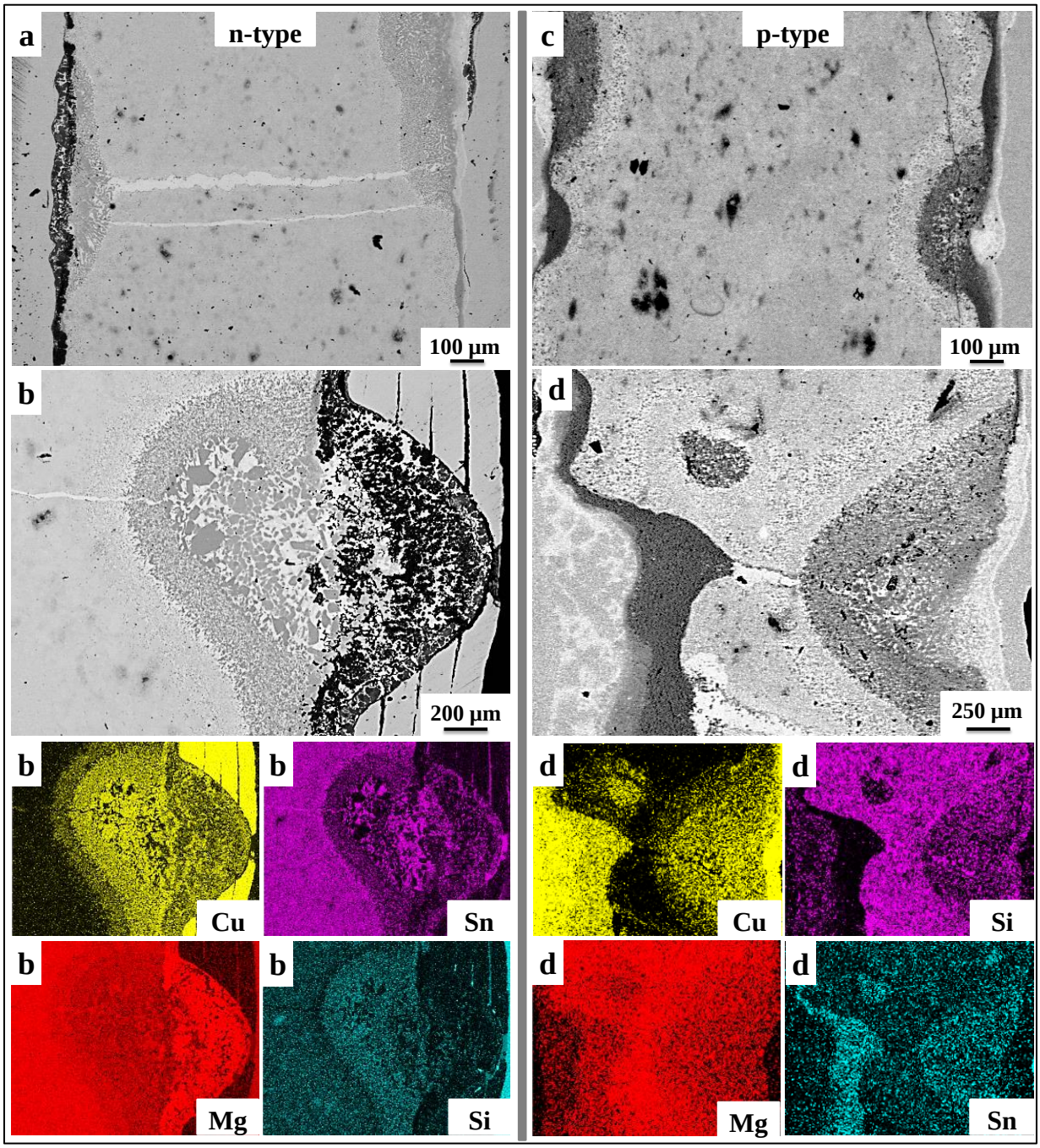

Figure 6: *SEM pictures of annealed Cu joined $Mg_2Si_{0.3}Sn_{0.7}$: (a): overview of joint n-type, (b): EDX element mapping of localized n-type joined interface, (c): overview of joined p-type, (d): EDX element mapping of localized p-type joined interface*

Figure 6 shows the SEM results of annealed Cu-joint n- and p-type samples. At low magnification, the annealed n-type $Mg_2Si_{0.3}Sn_{0.7}$ looks similar to the non-annealed sample, but, as expected, the interface and the local diffusion zones have expanded respectively to ~ 250 µm and ~ 600 µm. Two bright lines joining the diffusion zones from the interfaces on both sides are visible in **Figure 6 (a)**. As it was taken in backscattering mode, the brightest regions are Sn-rich, Sn being the heaviest element.

One more interesting feature was also observed and is shown in **Figure 6 (b)** which is the diffusion of the TE material inside the Cu layers, causing a delamination of the foils.

EDX element mappings show that the microstructure and composition of the diffusion layers on the joint n-type interface remain almost the same after annealing: Cu dendrites agglomerate in a Sn-rich environment. The part that diffuses inside Cu is mostly Mg. Sn areas locally exist but Si is completely absent. Literature on inter-diffusion of Cu and Mg under temperatures $\sim 450°C$ [50] shows that the binary compositions Mg_2Cu and $MgCu_2$ occur. As the formation energy of Mg_2Cu is lower than that of $MgCu_2$, the former binary compound would form before the latter. This could explain the higher concentration of Mg diffused in Cu.

The annealed Cu-joined p-type sample on **Figure 6 (c)** shows also stronger diffusion, similar to n-type, with diffusion zones $\sim 200\ \mu m$ thickness. One crack can also be seen inside the sample parallel to the interface.

Figure 6 (d) shows very thick localized diffusion zones $\sim 450\ \mu m$ each, where Cu has penetrated far inside the material from both sides. From the difference in greyscale, the diffusion zones seem to have different compositions, but as general overview, they both seem to be mainly composed of Mg-Cu-Si phases in Sn-rich $Mg_2(Si,Sn)$ matrix.

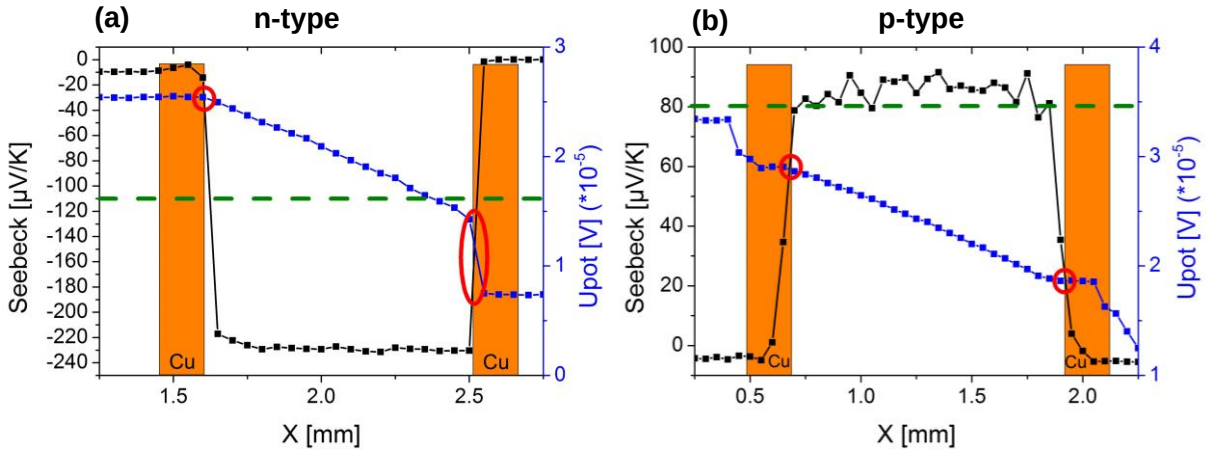

Figure 7: *PSM graphs of annealed (a): n- and (b): p-type Cu joined $Mg_2Si_{0.3}Sn_{0.7}$. The dashed green lines indicate the value of the sample´s Seebeck coefficients before joining.*

Figure 7 shows the Seebeck and potential graphs of the annealed samples. P-type samples still show no drop at the interfaces, indicating a low r_c. However, the potential line for n-type shows a large drop at the right-hand side interface, even though the left-hand side shows none. This indicates that changes have occurred at the interfaces under annealing, which caused the potential to drop. Another possibility could be that the scanned region had cracks or localized delamination between Cu and the TE material.

The averaged results using $Eq.3$ and $Eq.7$ are displayed in **Table 5**. As expected from the PSM graphs in **Figure 7**, r_c is low for p-type. For n-type, the final averaged r_c has been disentangled for interfaces on both sides.

***Table 5**: Specific contact resistance values of annealed n- and p-type $Mg_2Si_{0.3}Sn_{0.7}$ joined with Cu (450°C, 1 week)*

Sample	$r_c(Eq.7)$ / $(\mu\Omega cm^2)$	r_c $(Eq.3)$ / $(\mu\Omega cm^2)$
Annealed n + Cu (left side)	11 ± 6	13 ± 7
Annealed n + Cu (right side)	155 ± 30	181 ± 30
Annealed p + Cu	7 ± 5	6 ± 4

Similar to the non-annealed case, S of n-type changed to $\sim -230\,\mu V/K$. Here again, new measurements for σ_{TE} have been obtained and implemented in $Eq.7$. Here also, we provide estimations for the carrier concentrations (using $\boldsymbol{m_D^*} = 2.5$ [49] for n-type and $\boldsymbol{m_D^*} = 1.5$ for p-type [29]) as well as ratios of electrical contact resistances to total resistances in **Table 6**.

***Table 6**: Seebeck coefficients S, estimated carrier concentrations n and ratios of contact resistance to material resistance for contacted samples.*

Sample	S $(\mu V/K)$	n (cm^{-3})	σ (S/cm)	r_c $(\mu\Omega cm^2))$	R_{TE} $(\times 10^{-4}\Omega)$	$2r_c/(A \times R_{TE})$
n + Cu (left side)	-230	5.5×10^{19}	450	11 ± 6	11.1	1.98 %
n + Cu (right side)				155 ± 30		27.92 %
p + Cu	80	2.35×10^{20}	683	7 ± 5	4.39	3.19 %

It can be seen that the resistance ratio remains small also after annealing, with the exception of the right side of the n + Cu sample.

IV. **Discussion**

Results for n- and p-type $Mg_2Si_{0.3}Sn_{0.7}$ contacted with Cu and $Ni_{45}Cu_{55}$ electrodes are presented. Both electrodes showed mechanically stable joining to both material types, with no delamination. SEM/EDX investigations show Cu diffusion into n- and p-types, resulting in thick inhomogeneous reaction layers and diffusion zones of complex structures. These diffusion layers contain dendrites of Cu growing into a Sn-rich matrix, which occurred due to heterogeneous nucleation. In fact, heterogeneous nucleation, which is common in solid solutions, occurs at phase boundaries or around

impurities, initiating the growth process of the dendrites [51]. In our case, the dendritic growth presumably initiates as Cu diffuses along the grain boundaries [52-53] and grows due to the temperature gradient caused by the local heating under direct joining current, which disturbs the equilibrium conditions.

The composition and microstructure of the diffusion zones are different. In both n- and p-type cases, the ternary phases γ ($Cu_{51.7}Mg_{33.3}Sn_{15}$) and τ_1 ($Cu_{1.5}MgSi_{0.5}$) exist, but with different layering order and different thicknesses. The size and distribution of the dendrites are also different. While some thickness variation of the interface layer is often observed, comparison with literature [15, 28] indicates that the combination of Cu and Sn is responsible for the strong variations observed in our Sn-rich samples, as Cu and Sn tend to form various phases a wide range of temperatures and concentrations[54].

Similar diffusion behaviour was observed in joining with $Ni_{45}Cu_{55}$, except for the difference in interface thicknesses on both sides of each sample. This could be explained by the direct current running through the materials inside the sintering die. In fact, the (technical) current runs through the samples from bottom to top, which would favor the electromigration of Ni and Cu cations in that particular direction. Therefore, the thicker interfaces would be on the bottom side of the joint samples, while the thinner ones would be on top. As such behavior was not observed with Cu-joining, Ni is expected to play an important part in this electromigration process. It is carried by the current from the electrode to the sample, but it acts as a diffusion barrier to Cu when the diffusion happens in the opposite direction of the current flow [55]. In fact, Ni, but also metallic silicide materials (Ni-Si in this case) are known to be good barriers to Cu diffusion [53, 56-57]. The difference in joining temperatures with Cu and $Ni_{45}Cu_{55}$ (600 °C and 550 °C respectively) is another possible explanation that cannot be excluded [28].

For both electrodes, inhomogeneous diffusion occurred, leading to different reactions with the TE material, and the formation of new phases with new properties. Even though some diffusion is preferred as it helps the adhesion of the electrode to the TE material, too much diffusion would cause a loss of the initial functional material with the desired TE properties. The new resulting phases would also bring new CTE values into play, which increases the risk of higher CTE mismatches and hence results in further cracks under thermal cycling.

Local potential and Seebeck mapping were used to determine the specific electrical contact resistance. r_c was low (< 10 μΩ.cm^2) for Cu joint with both n- and p-types, indicating that the interfaces are mainly composed of conductive phases that do not hinder the current flow. As Cu has a CTE that matches the CTE of $Mg_2(Si,Sn)$ solid solutions better than that of the binary Mg_2Si, such good contacting was expected. This also proves the prediction of Cai et al. [15] that doped $Mg_2(Si,Sn)$ would work better than undoped Mg_2Si, which had a quite high contact resistance (r_c = 13.7 mΩcm^2) when joined with Cu. However, despite the differences in CTE, no cracks were observed in both the

solid solution and the binary cases, indicating that the CTE mismatch is not the only relevant criterion of choice for contacting electrodes. In fact, it seems as if the order is also important, with the preferred case of the electrode having the higher CTE.

The r_c values of Cu joint $Mg_2Si_{0.3}Sn_{0.7}$ are also lower than those obtained from Ni and Ag joining [28]. Even though Ag joint with p-type $Mg_2Si_{1-x}Sn_x$ at 450 °C had a low contact resistance (< 10 μΩcm^2), results with n-type were higher. Such behaviour was correlated with the fact that, as Ag is a p-type dopant, unexpected p-type doping occurred close to the Ag/n-type interface, resulting in a carrier density depletion area which led to the higher contact resistance.

On the other hand, values for samples joined with $Ni_{45}Cu_{55}$ were higher for p-type and with higher uncertainty for n-type, due to the different interfaces in the reaction layers and the metallic channels connecting the interfaces, respectively. Previous studies on Ni joining reported that Ni was a good contacting solution for Mg_2Si, with low r_c (< 10 μΩcm^2) [13-14], but it was not a good option for the solid solution, as cracks have developed due to the CTE mismatch and local r_c values were somewhat higher (~ 35 μΩcm^2) [28]. From that perspective, $Ni_{45}Cu_{55}$ was expected to have better contacting results than Ni. However, as the CTE of $Ni_{45}Cu_{55}$ still does not perfectly match that of $Mg_2Si_{0.3}Sn_{0.7}$, some cracks still occurred.

After contacting, a change in S values from $-110\mu V/K$ to $-160\mu V/K$, and therefore a change in carrier concentration, was observed for the case of n-type samples joined with both Cu and $Ni_{45}Cu_{55}$, while they remained unchanged ($\sim 85\ \mu V/K$) for p-type. No clear explanation to this behaviour has been obtained so far. However, one hypothesis is the difference in Si and Sn ratio (30:70 for p, 30:66.5 for n), though very small, between both material types as Bi substitutes Sn in n-type. Another possible cause could be the difference in Mg content, as n-type materials are made with 3% excess Mg, but also Li substitutes Mg in p-type materials. The dopants themselves could also add to this observed difference in behaviour. As similar results were observed in $Mg_2(Si,Sn)$ joined with Ag [28], it is clear that we have a carrier type dependence of the behaviour of the $Mg_2Si_{1-x}Sn_x$ material system which needs to be studied further.

Annealing experiments were carried out at 450°C during one week for Cu joining to study the thermal stability and the development of r_c. As expected, the diffusion of Cu was intensified, which affected the contact resistance and is expected to change the material properties on the long run. r_c values remained relatively low ($<$ 10 μΩcm^2) for p-type after annealing, while n-type samples show a different behaviour. In fact, the averaged contact resistance was quite high because of the sudden potential drop on one side of the sample (**Figure 7 (a)**). This can be correlated with both the changes in interfaces at diffusion zones and the delamination that was observed due to the inter-diffusion of Mg and Cu. In fact, in case of foil delamination, extra resistance terms at each interface would be

added (foil to foil, or foil to TE material), and due to the limited spatial resolution of the PSM, these added resistances are picked up as part of the total contact resistance, leading to high r_c values.

The Seebeck value has also changed for n-type after annealing, reaching a value of $-230\ \mu V/K$, which did not happen with p-type. We then observe a clear dependence of the change in material properties, and thus contact resistances, on the dominant carrier type, similarly to what was observed for Ag [28] with $Mg_2(Si,Sn)$. A dependence of interface properties on dominant carrier type has also been reported for the Bi_2-Te_3 system where n-type $Bi_2Te_{2.7}Se_{0.3}$ and p-type $Bi_{0.4}Sb_{1.6}Te_3$ showed different behaviours at the interfaces when joined with Ni [58]. Whether this is due to (local) changes in the composition or is related to defects in the material requires further investigations. However, as such change in TE properties did not happen after annealing non-contacted $Mg_2Si_{0.3}Sn_{0.7}$ at 450°C for one month [33], it can be safely assumed that the observable changes here are due to contacting and continuous inhomogeneous diffusion, and not only annealing.

V. Conclusion

In this work, contacting of n- and p- type $Mg_2Si_{0.3}Sn_{0.7}$ with Cu and $Ni_{45}Cu_{55}$ electrodes was investigated. Both electrodes have shown stable contacting and adhesion with no delamination. Strong diffusion of both metals was observable inside the TE material, resulting in complex interfaces and thick diffusion zones. The specific electrical contact resistance r_c was low for Cu ($< 10\ \mu\Omega cm^2$) but higher for $Ni_{45}Cu_{55}$ ($< 50\ \mu\Omega cm^2$), which could be a result of the cracks that occurred due to a higher CTE mismatch.

The stability of the Cu contacting has been tested by annealing the joined samples for one week under a temperature of 450°C. The obtained results show a stronger diffusion of Cu, and even a diffusion of the TE material into the electrode, which caused local delamination. Moreover, the specific contact resistance r_c remained relatively low, except for one case where the delamination occurred. However, the diffusion changed the microstructure and the thermoelectric properties of the n-type material, which does not guarantee optimized properties anymore, possibly reducing zT and TE efficiency. Therefore, the diffusion needs to be controlled in order for Cu to be a potential technological contacting solution. Sputtering of a thin diffusion barrier layer is a possible option to remediate this issue.

Finally, the results of this work show that CTE match is not the only criterion for electrode material selection. Though necessary, it appears like there is a favourable order in the CTE comparability ($CTE_{electrode} \geq CTE_{TE\ material}$ better than $CTE_{electrode} \leq CTE_{TE\ material}$). It is also important to consider the

phases in the reaction layer as well as potential interactions between electrode and TE material. As we have shown here, these can depend on the dominant carrier type of the TE material.

Conflicts of interest

The authors declare no competing financial interest.

Acknowledgements

The authors would like to gratefully acknowledge the endorsement for the DLR executive Board Members for Space Research and Technology, as well as the financial support from the Young Research Group Leader Program. G.C.H would like to thank the financial support of the Mexican Science and Technology Ministry (CONACyT), and N.F and N.H.P would like to thank the DAAD fellowship programs No. 248 and 57265854, respectively. Lastly, we would also like to acknowledge Pawel Ziolkowski and Przemyslaw Blaschkewitz for their help and assistance with the thermoelectric measurements.

References:

(1) Bell, L. E. Cooling, heating, generating power, and recovering waste heat with thermoelectric systems. *Science* **2008,** *321* (5895), 1457-1461.
(2) Tritt, T. M. Thermoelectric phenomena, materials, and applications. *Annual review of materials research* **2011,** *41*, 433-448.
(3) DiSalvo, F. J. Thermoelectric cooling and power generation. *Science* **1999,** *285* (5428), 703-706.
(4) Aswal, D. K.; Basu, R.; Singh, A. Key issues in development of thermoelectric power generators: High figure-of-merit materials and their highly conducting interfaces with metallic interconnects. *Energy conversion and management* **2016,** *114*, 50-67.
(5) Priya, S.; Inman, D. J. *Energy harvesting technologies*, Springer: 2009; Vol. 21.
(6) Rowe, D. M. Conversion Efficiency and Figure-of-Merit. In *CRC Handbook of Thermoelectrics*; CRC press: 1995; pp 31-37.
(7) Liu, W.; Jie, Q.; Kim, H. S.; Ren, Z. Current progress and future challenges in thermoelectric power generation: From materials to devices. *Acta Materialia* **2015,** *87*, 357-376.
(8) Luo, A. A. In *Recent magnesium alloy development for automotive powertrain applications*, Materials Science Forum, Trans Tech Publ: 2003; pp 57-66.
(9) Santos, R.; Yamini, S. A.; Dou, S. X. Recent progress in magnesium-based thermoelectric materials. *Journal of Materials Chemistry A* **2018,** *6* (8), 3328-3341.
(10) Zaitsev, V. K.; Isachenko, G. N.; Burkov, A. T. Efficient Thermoelectric Materials Based on Solid Solutions of Mg2X Compounds (X= Si, Ge, Sn). In *Thermoelectrics for Power Generation-A Look at Trends in the Technology*; InTech: 2016.
(11) Ferrario, A.; Battiston, S.; Boldrini, S.; Sakamoto, T.; Miorin, E.; Famengo, A.; Miozzo, A.; Fiameni, S.; Iida, T.; Fabrizio, M. Mechanical and electrical characterization of low-resistivity contact materials for Mg2Si. *Materials Today: Proceedings* **2015,** *2* (2), 573-582.
(12) Sakamoto, T.; Taguchi, Y.; Kutsuwa, T.; Ichimi, K.; Kasatani, S.; Inada, M. Investigation of barrier-layer materials for Mg 2 Si/Ni interfaces. *J Electron Mater* **2016,** *45* (3), 1321-1327.
(13) de Boor, J.; Gloanec, C.; Kolb, H.; Sottong, R.; Ziolkowski, P.; Müller, E. Fabrication and characterization of nickel contacts for magnesium silicide based thermoelectric generators. *Journal of Alloys and Compounds* **2015,** *632*, 348-353.

(14) de Boor, J.; Droste, D.; Schneider, C.; Janek, J.; Mueller, E. Thermal stability of magnesium silicide/nickel contacts. *J Electron Mater* **2016,** *45* (10), 5313-5320.
(15) Cai, L.; Li, P.; Wang, P.; Luo, Q.; Zhai, P.; Zhang, Q. Duration of Thermal Stability and Mechanical Properties of Mg 2 Si/Cu Thermoelectric Joints. *J Electron Mater* **2018,** *47* (5), 2591-2599.
(16) Ngan, P. H.; Christensen, D. V.; Snyder, G. J.; Hung, L. T.; Linderoth, S.; Nong, N. V.; Pryds, N. Towards high efficiency segmented thermoelectric unicouples. *physica status solidi (a)* **2014,** *211* (1), 9-17.
(17) de Boor, J.; Dasgupta, T.; Saparamadu, U.; Müller, E.; Ren, Z. Recent progress in p-type thermoelectric magnesium silicide based solid solutions. *Materials Today Energy* **2017,** *4*, 105-121.
(18) Bashir, M. B. A.; Said, S. M.; Sabri, M. F. M.; Shnawah, D. A.; Elsheikh, M. H. Recent advances on Mg2Si1− xSnx materials for thermoelectric generation. *Renewable and Sustainable Energy Reviews* **2014,** *37*, 569-584.
(19) de Boor, J.; Saparamadu, U.; Mao, J.; Dahal, K.; Müller, E.; Ren, Z. Thermoelectric performance of Li doped, p-type Mg 2 (Ge, Sn) and comparison with Mg 2 (Si, Sn). *Acta Materialia* **2016,** *120*, 273-280.
(20) Zaitsev, V.; Fedorov, M.; Gurieva, E.; Eremin, I.; Konstantinov, P.; Samunin, A. Y.; Vedernikov, M. Highly effective Mg 2 Si 1− x Sn x thermoelectrics. *Physical Review B* **2006,** *74* (4), 045207.
(21) Fedorov, M. I.; Zaitsev, V. K.; Isachenko, G. N. In *High effective thermoelectrics based on the Mg2Si-Mg2Sn solid solution*, Solid State Phenomena, Trans Tech Publ: 2011; pp 286-292.
(22) Liu, W.; Tan, X.; Yin, K.; Liu, H.; Tang, X.; Shi, J.; Zhang, Q.; Uher, C. Convergence of conduction bands as a means of enhancing thermoelectric performance of n-type Mg 2 Si 1− x Sn x solid solutions. *Physical review letters* **2012,** *108* (16), 166601.
(23) Liu, W. D.; Chen, Z. G.; Zou, J. Eco-Friendly Higher Manganese Silicide Thermoelectric Materials: Progress and Future Challenges. *Advanced Energy Materials* **2018,** *8* (19), 1800056.
(24) Girard, S. N.; Chen, X.; Meng, F.; Pokhrel, A.; Zhou, J.; Shi, L.; Jin, S. Thermoelectric properties of undoped high purity higher manganese silicides grown by chemical vapor transport. *Chemistry of Materials* **2014,** *26* (17), 5097-5104.
(25) Skomedal, G.; Holmgren, L.; Middleton, H.; Eremin, I.; Isachenko, G.; Jaegle, M.; Tarantik, K.; Vlachos, N.; Manoli, M.; Kyratsi, T. Design, assembly and characterization of silicide-based thermoelectric modules. *Energy conversion and management* **2016,** *110*, 13-21.
(26) Kim, H. S.; Kikuchi, K.; Itoh, T.; Iida, T.; Taya, M. Design of segmented thermoelectric generator based on cost-effective and light-weight thermoelectric alloys. *Materials Science and Engineering: B* **2014,** *185*, 45-52.
(27) Nakamura, T.; Hatakeyama, K.; Minowa, M.; Mito, Y.; Arai, K.; Iida, T.; Nishio, K. Power-Generation Performance of a π-Structured Thermoelectric Module Containing Mg 2 Si and MnSi 1.73. *J Electron Mater* **2015,** *44* (10), 3592-3597.
(28) Pham, N. H.; Farahi, N.; Kamila, H.; Sankhla, A.; Ayachi, S.; Müller, E.; and; Boor, J. d. Contact development for p- and n-type Mg2Si1-xSnx thermoelectric generator using Ni

and Ag. *Materials Today Energy* **2018**.
(29) Kamila, H.; Sahu, P.; Sankhla, A.; Yasseri, M.; Pham, H.-N.; Dasgupta, T.; Mueller, E.; de Boor, J. Analyzing transport properties of p-type Mg 2 Si–Mg 2 Sn solid solutions: optimization of thermoelectric performance and insight into the electronic band structure. *Journal of Materials Chemistry A* **2019,** *7* (3), 1045-1054.
(30) Rogl, G.; Zhang, L.; Rogl, P.; Grytsiv, A.; Falmbigl, M.; Rajs, D.; Kriegisch, M.; Müller, H.; Bauer, E.; Koppensteiner, J. Thermal expansion of skutterudites. *Journal of applied physics* **2010,** *107* (4), 043507.
(31) *Handbook of Chemistry and Physics*, 55 ed.; CRC Press: USA, 1974.
(32) Davis, J. R. *Copper and copper alloys*, ASM international: 2001.
(33) Farahi, N.; Stiewe, C.; Truong, D. N.; de Boor, J.; Müller, E. High efficiency Mg 2 (Si, Sn)-based thermoelectric materials: scale-up synthesis, functional homogeneity, and thermal stability. *RSC Advances* **2019,** *9* (40), 23021-23028.

(34) Sankhla, A.; Patil, A.; Kamila, H.; Yasseri, M.; Farahi, N.; Mueller, E.; de Boor, J. Mechanical Alloying of Optimized Mg2 (Si, Sn) Solid Solutions: Understanding Phase Evolution and Tuning Synthesis Parameters for Thermoelectric Applications. *ACS Applied Energy Materials* **2018,** *1* (2), 531-542.
(35) Kamila, H.; Yasseri, M.; Pham, N.; Farahi, N.; Müller, E.; de Boor, J. Synthesis of p-type Mg2Si1-xSnx with x= 0-1 and optimization of the synthesis parameters. *Materials Today: Proceedings* **2019,** *8*, 546-555.
(36) de Boor, J.; Stiewe, C.; Ziolkowski, P.; Dasgupta, T.; Karpinski, G.; Lenz, E.; Edler, F.; Mueller, E. High-temperature measurement of Seebeck coefficient and electrical conductivity. *J Electron Mater* **2013,** *42* (7), 1711-1718.
(37) Yasseri, M.; Farahi, N.; Kelm, K.; Mueller, E.; de Boor, J. Rapid determination of local composition in quasi-binary, inhomogeneous material systems from backscattered electron image contrast. *Materialia* **2018**.
(38) Bochvar, N.; Lysova, E.; Rokhlin, L. *Cu-Mg-Si (Copper - Magnesium - Silicon): Datasheet from Landolt-Börnstein - Group IV Physical Chemistry · Volume 11A4: "Light Metal Systems. Part 4" in SpringerMaterials (https://dx.doi.org/10.1007/11008514_19)*, Springer-Verlag Berlin Heidelberg.
(39) Rokhlin, L.; Lysova, E. *Cu-Mg-Sn (Copper - Magnesium - Tin): Datasheet from Landolt-Börnstein - Group IV Physical Chemistry · Volume 11A4: "Light Metal Systems. Part 4" in SpringerMaterials (https://dx.doi.org/10.1007/11008514_20)*, Springer-Verlag Berlin Heidelberg.
(40) Nash, P.; Nash, A. The Ni− Si (Nickel-Silicon) system. *Bulletin of Alloy Phase Diagrams* **1987,** *8* (1), 6-14.
(41) Platzek, D.; Karpinski, G.; Stiewe, C.; Ziolkowski, P.; Drasar, C.; Muller, E. In *Potential-Seebeck-microprobe (PSM): measuring the spatial resolution of the Seebeck coefficient and the electric potential*, Thermoelectrics, 2005. ICT 2005. 24th International Conference on, IEEE: 2005; pp 13-16.
(42) Chen, K.; Fan, A.; Tan, C.; Reif, R. Contact resistance measurement of bonded copper interconnects for three-dimensional integration technology. *IEEE Electron Device Letters* **2004,** *25* (1), 10-12.
(43) Schroder, D. K. *Semiconductor material and device characterization*, John Wiley & Sons: 2006.
(44) Nakamura, S.; Mori, Y.; Takarabe, K. i. Analysis of the Microstructure of Mg 2 Si Thermoelectric Devices. *J Electron Mater* **2014,** *43* (6), 2174-2178.
(45) Thimont, Y.; Lognoné, Q.; Goupil, C.; Gascoin, F.; Guilmeau, E. Design of apparatus for Ni/Mg 2 Si and Ni/MnSi 1.75 contact resistance determination for thermoelectric legs. *J Electron Mater* **2014,** *43* (6), 2023-2028.
(46) Snyder, G. J.; Toberer, E. S. Complex thermoelectric materials. In *Materials For Sustainable Energy: A Collection of Peer-Reviewed Research and Review Articles from Nature Publishing Group*; World Scientific: 2011; pp 101-110.
(47) Liu, W.; Chi, H.; Sun, H.; Zhang, Q.; Yin, K.; Tang, X.; Zhang, Q.; Uher, C. Advanced thermoelectrics governed by a single parabolic band: Mg 2 Si 0.3 Sn 0.7, a canonical example. *Physical Chemistry Chemical Physics* **2014,** *16* (15), 6893-6897.
(48) de Boor, J.; Gupta, S.; Kolb, H.; Dasgupta, T.; Mueller, E. Thermoelectric transport and microstructure of optimized Mg2Si0. 8Sn0. 2. *Journal of Materials Chemistry C* **2015,** *3* (40), 10467-10475.
(49) Farahi, N.; Prabhudev, S.; Botton, G. A.; Salvador, J. R.; Kleinke, H. Nano-and microstructure engineering: an effective method for creating high efficiency magnesium silicide based thermoelectrics. *ACS applied materials & interfaces* **2016,** *8* (50), 34431-34437.
(50) Dai, J.; Jiang, B.; Zhang, J.; Yang, Q.; Jiang, Z.; Dong, H.; Pan, F. Diffusion kinetics in Mg-Cu binary system. *Journal of Phase Equilibria and Diffusion* **2015,** *36* (6), 613-619.
(51) Liu, X. Heterogeneous nucleation or homogeneous nucleation? *The Journal of Chemical Physics* **2000,** *112* (22), 9949-9955.
(52) Wang, S.-Q. Barriers against copper diffusion into silicon and drift through silicon dioxide. *MRS bulletin* **1994,** *19* (8), 30-40.

(53) Liu, B.; Yang, L.; Li, X.; Wang, K.; Guo, Z.; Chen, J.; Li, M.; Zhao, D.; Zhao, Q.; Zhang, X. Ultrathin amorphous Ni–Ti film as diffusion barrier for Cu interconnection. *Applied Surface Science* **2011,** *257* (7), 2920-2922.
(54) Fürtauer, S.; Li, D.; Cupid, D.; Flandorfer, H. The Cu–Sn phase diagram, Part I: new experimental results. *Intermetallics* **2013,** *34*, 142-147.
(55) Kale, A.; Beese, E.; Saenz, T.; Warren, E.; Nemeth, W.; Young, D.; Marshall, A.; Florent, K.; Kurinec, S. K.; Agarwal, S. In *Study of nickel silicide as a copper diffusion barrier in monocrystalline silicon solar cells*, Photovoltaic Specialist Conference (PVSC), 2017 IEEE 44th, IEEE: 2017; pp 1-4.
(56) Min, S. K.; Kim, D. H.; Lee, S. H. Nickel silicide for Ni/Cu contact mono-silicon solar cells. *Electronic Materials Letters* **2013,** *9* (4), 433-435.
(57) Yang, L.; Wang, S. J.; Huo, J. C.; Li, X. H.; Guo, J. X.; Dai, X. H.; Ma, L. X.; Zhang, X. Y.; Liu, B. T. INVESTIGATION OF Ta/Ni–Al INTEGRATED FILM USED AS A DIFFUSION BARRIER LAYER BETWEEN Cu AND Si. *Surface Review and Letters* **2014,** *21* (06), 1450079.
(58) Liu, W.; Wang, H.; Wang, L.; Wang, X.; Joshi, G.; Chen, G.; Ren, Z. Understanding of the contact of nanostructured thermoelectric n-type Bi 2 Te 2.7 Se 0.3 legs for power generation applications. *Journal of Materials Chemistry A* **2013,** *1* (42), 13093-13100.

Graphic Abstract: